Formation and persistence of glaciovolcanic voids explored with analytical and numerical models: Supplementary Material

Tryggvi Unnsteinsson[1], Gwenn E. Flowers[1] and Glyn Williams-Jones[1]

[1]*Department of Earth Sciences, Simon Fraser University, 8888 University Drive, Burnaby, British Columbia, V5A 1S6*

Correspondence: Tryggvi Unnsteinsson <tryggvi_unnsteinsson@sfu.ca>

OBSERVED EVOLUTION OF GLACIOVOLCANIC VOIDS IN JOB GLACIER

The glaciovolcanic chimneys that were observed in July 2016 within Job Glacier on *Qẇelqẇelústen* or the Mount Meager Volcanic Complex, British Columbia, Canada, likely did not spring into existence immediately prior to their discovery. One of the chimneys can be seen on Planet satellite imagery from 2015 (Planet Team, 2015).

Initial accounts in 2016 of the glaciovolcanic chimneys, describe two active vents, here labelled 1a and 2a, and one possibly inactive, 3a (Williams-Jones, 2016) (Fig. 1). Up until 2020, chimneys 1a and 2a acted as perennial features, while the activity in 3a seemed to fluctuate more, temporarily opening and closing over time (Fig. 1). Chimneys 1a and 3a were seemingly stationary, but the opening of 2a was advected with ice flow some 50 m downstream between 2016 and 2019. In summer of 2020, a new chimney appeared directly upstream of 2a, which in turn had shown decreased degassing activity, eventually becoming nearly inactive by the end of summer. We therefore hypothesise that 2a had been advected into a thermal state in which it could not maintain itself. Thus, the inevitable closure of 2a must have initiated the formation of a new chimney, hence labelled 2b, directly above its geothermal source. Chimney 2b, however, formed a few tens of metres further upstream from where 2a was initially discovered, so a relocation of fumaroles or initiation of new ones cannot be ruled out. In summer of 2021, British Columbia was affected by an unprecedented heat wave which had a devastating effect on glaciers in the region (e.g., White and others, 2023). During that summer, at least three new glaciovolcanic voids were observed: 3b, 4a, and 5a in Fig.

1. It is highly probable that the elevated surface melt rates facilitated the formation or expression of the new glaciovolcanic features.

Aside from a few small-scale geophysical surveys, the only data available to constrain the complex glaciovolcanic interactions taking place within Job Glacier are map products and photographs. Based on photographs and personal accounts, Chimneys 1a and 2a were close to vertical when they were observed in 2016. Since then, Chimney 1a has widened, and the surface around it, especially downstream, has been subject to significant lowering. In 2020, bedrock could be seen at the base of Chimney 1a which is now transforming into a small nunatak in the glacier.

Chimney 2a has undergone more interesting development since 2016. Over the years, the mouth of Chimney 2a was slowly advected down glacier and the entrance became less steep. In 2019, exploration revealed parts of the chimney to be near horizontal (personal communication from C. Stenner, 2020). In 2020, a new chimney, 2b, formed directly upstream of 2a. The new chimney can be seen in 7 June 2020 Sentinel-2 images (Modified Copernicus Sentinel data, 2020/Sentinel Hub), but the onset timing of its surface expression is uncertain. A shadow that possibly indicates either subsidence in the snow cover, or even an opening above the location of the new chimney is observable in Sentinel-2 images in February 2019 or possibly even as early as of November 2019. The earliest photograph of the new chimney is from 7 April 2020, and a field trip in August 2020 confirmed that Chimney 2a and 2b were separate entities. Chimney 2a was seemingly still partially active at that point, but had not been fully cleared of snow from the previous winter. Chimney 2b was vertical just like 2a was when it was first discovered. We propose, based on the discovery, that a chimney could be advected into an unstable thermal state, forcing its closure and the formation of a new one above the original geothermal source. An unstable thermal state occurs when the surface area of a chimney which has been elongated due to glacier flow, becomes too large for the geothermally induced melt to keep up with creep closure and blockages. These observations inspire the choice of physical processes that we attempt to represent in the physics-based conceptual model.

The glaciovolcanic feature labelled 3a is more difficult to place into a category based on its geometry. When first observed, it was merely localised subsidence that occasionally opened up and exhibited limited activity. After the heat wave in summer 2021, it had melted down to bedrock where two caves, 3a and 3b, could be seen linked together. Similarly, Chimney 5a opened up after the heat wave and is most likely connected to Cave 3b. It is therefore possible that Chimney 5a may have formed as the fumarole(s) of Cave 3b exploited weaknesses (i.e., crevasses) in the ice directly above.

Chimney 4a is similar to Chimneys 2a and 2b in shape and form. The main difference is that the mouth of 4a is more like that of a cave, similar to 2a at the end of its existence. The floor of 4a, however, looks like it drops quite sharply once inside.

In addition to the direct loss of ice associated with the formation of the chimneys, the glacier downstream of the chimneys is also affected. The glacier surface several tens of meters downstream of Chimneys 1a and 2b has been subjected to increased lowering relative to the surface beside and upstream of the chimneys. There exist no estimates of the magnitude of increased down-slope surface lowering due to the presence of the chimneys, as the only data available are various photographs taken by scientists and tourists. Three mechanisms likely contribute to the increased down-slope lowering: (i) a conversion to a gravitationally driven flow of the geothermal gases (Williams-Jones and Rymer, 2015) once above the glacier surface, contributing excess heat to ablation; (ii) the chimneys inhibit ice advection from areas upstream of the chimney as the incoming ice is melted by the geothermal source; and (iii) geothermally induced melting at the glacier bed results in surface lowering. It was attempted in summer of 2021 to quantify the excess surface melt with ablation stakes, but the stakes melted out before the final measurements could be made. The effect of the other two mechanisms would have to be quantified by modelling the features, while accounting for all terms in the continuity equation, including ice flux, accumulation and supra- and subglacial ablation.

In September of 2018, an ice-penetrating radar survey was conducted on Job Glacier to measure ice thickness (Warwick, 2020). Five short transects were measured near Chimneys 1a and 2a, finding a maximum ice thickness of 105 m, but closest to the chimneys the ice was < 80 m thick (Warwick, 2020). Another source of ice thickness data are the global inversion datasets of Farinotti and others (2019) and Millan and others (2022).

NUMERICAL MODELS OF ANALYTICAL CAVE GEOMETRIES

A full-Stokes numerical ice-flow model, Elmer/Ice (Gagliardini and others, 2013), was used to verify our analytically derived cave geometries (solid lines in Fig. 4a), and to compare with radially symmetric geometries (dashed lines in Fig. 4a). The model domain was set as the geometries in Fig. 4a, but extended to a width and height equal to the ice thickness H. The domain was then specified to be symmetrical around the z-axis. No-flux boundary conditions were applied to the bed, $y = 0$, and outer boundary, $x = H$, and the glacier surface was set as stress free. A diagnostic model simulation was then run to determine the closure rates at both the derived and radially symmetric cave surfaces (solid lines in Fig.

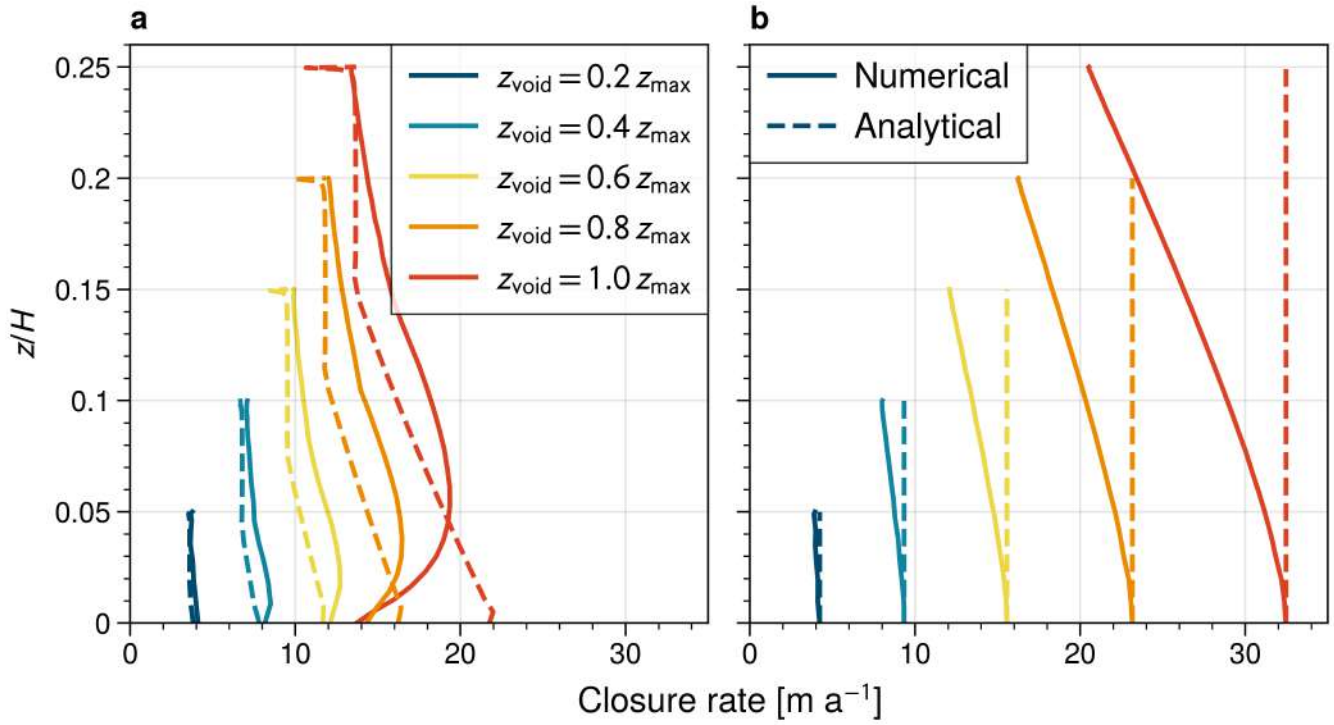

Fig. S1. Numerically (solid lines) and analytically (dashed lines) modelled closure rates normal to the surface of (**a**) the new cave geometries, given by equation Eqn. (7), and (**b**) radially symmetric ones. Results are given for geometries of five fractions of the maximum void height $z_{\max} = H/4$.

S1). The theoretical closure rates for the derived and radially symmetric cave geometries are given by Eqs. (5) and (2), respectively. However, the theoretical closure rates are an underestimate compared to those given by the numerical model. To make a meaningful comparison, the theoretical closure rates are adjusted by a factor such that the numerical and theoretical closure rates at the base of the radially symmetric caves match (dashed lines in Fig. S1). It can be seen that our derived geometries yield closure rates much more resembling the numerical results (Fig. S1a) than those of the radially symmetric geometries (Fig. S1b).

GLACIOVOLCANIC CHIMNEY EVOLUTION

If $\mathcal{C}(\mathcal{Z}, t)$ is the chimney centreline position at time t, then the centreline position after time Δt is given by

$$\mathcal{C}(\mathcal{Z}, t + \Delta t) = \mathcal{C}(\mathcal{Z}, t) + v_{\mathcal{X}}(\mathcal{Z})\,\Delta t, \tag{S1}$$

while the radius, R, remains constant. The chimney length, $\mathcal{L}(t)$, at time t is thus

$$\mathcal{L}(t) = \int_0^H \sqrt{1 + \left(\frac{\mathrm{d}\mathcal{C}(\mathcal{Z}, t)}{\mathrm{d}\mathcal{Z}}\right)^2}\,\mathrm{d}\mathcal{Z}, \tag{S2}$$

and the surface area of the chimney scales with its length as

$$\mathcal{S}(t) = 2\pi R\,\mathcal{L}(t). \tag{S3}$$

VOID-HEIGHT APPROXIMATION

We seek an analytical relationship to link the numerical model results and the input parameters. One way to consider steady state void geometries is to balance the growth and closure of the normalised void height $\tilde{h} = h/H$:

$$\frac{\mathrm{d}\tilde{h}}{\mathrm{d}t} = \left.\frac{\mathrm{d}\tilde{h}}{\mathrm{d}t}\right|_{\text{open}} + \left.\frac{\mathrm{d}\tilde{h}}{\mathrm{d}t}\right|_{\text{close}} = 0 \tag{S4}$$

We here assume that the closure rate of all voids is captured by the formulations of Nye (1953). We recognise that these do not accurately describe large voids, but neither do our analytical formulations above with incorporated depth dependency, thus the simple established version will be used here. For the

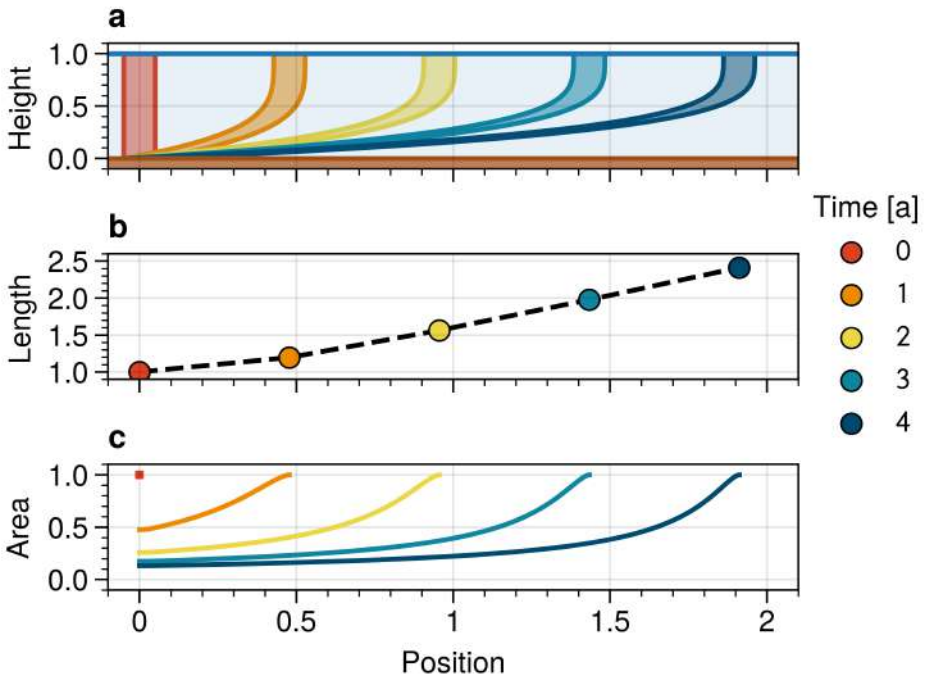

Fig. S2. Chimney evolution due to passive advection in parallel flow field with no creep closure and no sliding. (**a**) Chimney evolution in a parallel velocity field with a constant diameter. (**b**) Normalised length of the advected chimney, given by S2. (**c**) Normalised effective cross-sectional area, i.e., normal to the advected chimney surface. The flow field was computed for a driving stress of $\tau_d = 0.23\,\mathrm{MPa}$, i.e., shallow ice stress for a 100 m thick glacier on a bed slope of 15°. The colours indicate the position and geometry of the chimney at one year intervals.

melt opening Eqn. (3) it holds that

$$\left.\frac{\mathrm{d}\tilde{h}}{\mathrm{d}t}\right|_{\text{open}} \propto \dot{q}, \tag{S5}$$

and for the creep closure Eqn. (2) it is

$$\left.\frac{\mathrm{d}\tilde{h}}{\mathrm{d}t}\right|_{\text{close}} \propto H^n\,\tilde{h}. \tag{S6}$$

Inserting Eqs. (S5) and (S6) into Eqn. (S4) and rearranging then gives

$$\tilde{h} \propto H^{-n}\,\dot{q}. \tag{S7}$$

The specific heat flux $\dot{q}$ is a function of the void surface area, $\mathcal{S}$, which can approximated as a spherical cap for caves, $\mathcal{S}_{\text{cap}} = 2\pi r h$, where r and h are the void radius and height, respectively. Similarly for chimneys, the void surface area can be approximated as a cylinder, $\mathcal{S}_{\text{cylinder}} = 2\pi r h$, or a cone, $\mathcal{S}_{\text{cone}} = \pi\, r\, h \left(1 + (r/h)^2\right)^{1/2}$. For all of these surface approximations, it holds that $\mathcal{S} \propto r\, h$. We choose to reduce the proportionality to $\mathcal{S} \propto \tilde{h}$ as the radii of the modelled voids cannot be unambiguously and consistently defined across all void geometries. Since the definition of the specific heat flux is $\dot{q} \propto \dot{Q}/\mathcal{S}$, it then follows that $\dot{q} \propto \dot{Q}/\tilde{h}$. We thus get

$$\tilde{h}^2 \propto H^{-n}\,\dot{Q}, \tag{S8}$$

that is

$$\frac{h}{H} = a\, H^b\, \dot{Q}^c, \tag{14}$$

where theoretical values of the exponents are $b = -\frac{n}{2}$ and $c = \frac{1}{2}$, and the coefficient a, which is numerically fitted to Eqn. (14), has the units $\mathrm{m}^{-b}\mathrm{W}^{-c}$. There is no inherent slope dependence in Eqn. (14), but we assert that the coefficient a has a linear dependence to the sine of the slope angle α:

$$\frac{h}{H} = a_{\text{L1}}\,(1 + a_{\text{L2}}\,\sin(\alpha))\; H^b\, \dot{Q}^c, \tag{S9}$$

where coefficient a_{L1} has units $\mathrm{m}^{-b}\mathrm{W}^{-c}$ and a_{L2} is unitless.

This approach can be extended by considering the vertical velocity, v_z, along with the creep-closure rate in the vertical opening–closure balance

$$\frac{\mathrm{d}\tilde{h}}{\mathrm{d}t} = \left.\frac{\mathrm{d}\tilde{h}}{\mathrm{d}t}\right|_{\text{open}} + \left.\frac{\mathrm{d}\tilde{h}}{\mathrm{d}t}\right|_{\text{close}} + \tilde{v}_z(\tilde{h}) = 0. \tag{S10}$$

The bed-parallel velocity is given by the shallow-ice approximation, Eqn. (10). We set the vertical velocity to be equal to the vertical component of the first-order Taylor approximation of the bed-parallel velocity

$$\tilde{v}_z(\tilde{h}) = 2A \, \sin^{n+1}(\alpha) \, (\rho_i \, g \, H)^n \, \tilde{h}. \tag{S11}$$

Inserting Eqs. (S5), (S6) and (S11) into Eqn. (S10) and rearranging then yields

$$\tilde{h} \propto (1 + a_{P2} \, \sin^{n+1}(\alpha))^{-1} \, H^{-n} \, \dot{q}. \tag{S12}$$

Following the previous argument of $\dot{q} \propto \dot{Q}/\tilde{h}$ then yields

$$\tilde{h}^2 \propto (1 + a_{P2} \, \sin^{n+1}(\alpha))^{-1} \, H^{-n} \, \dot{Q}, \tag{S13}$$

and thus

$$\frac{h}{H} = a_{\mathrm{P1}} \, \left(1 + a_{\mathrm{P2}} \, \sin^{n+1}(\alpha)\right)^{-\frac{1}{2}} \, H^b \, \dot{Q}^c, \tag{S14}$$

where the theoretical values are $b = -\frac{n}{2}$ and $c = \frac{1}{2}$, and coefficient a_{P1} has the units $\mathrm{m}^{-b}\mathrm{W}^{-c}$, whereas a_{P2} is unitless. Note that this result is an equation of the form $h/H = aH^b\dot{Q}^c$, like Eqn. (14), which did not account for the ice velocity.

TAYLOR APPROXIMATION OF THE VERTICAL VELOCITY

To incorporate the ice velocity into the void-height approximation, we need a simplified expression of the vertical component of the velocity. The bed-parallel velocity, in the '$\mathcal{XYZ}$' coordinate system aligned with the glacier, and given by the shallow-ice approximation is

$$v_{\mathcal{X}}(\mathcal{Z}) = \frac{2A}{n+1} \, \tau_b^n \, H \, \left(1 - \left(1 - \frac{\mathcal{Z}}{H}\right)^{n+1}\right), \tag{S15}$$

where $\tau_b = \rho_i g H \sin(\alpha)$ is the basal shear stress (Cuffey and Paterson, 2010). We need to simplify Eqn. (S15) in terms of $\mathcal{Z}$, which can be done by using the Taylor series of the velocity profile. For the first term

in the Taylor series, the derivative of the velocity with respect to $\mathcal{Z}$ is:

$$\begin{aligned}\frac{\mathrm{d}v_{\mathcal{X}}}{\mathrm{d}\mathcal{Z}} &= \frac{2A}{n+1}\,\tau_b^n\,H\,\frac{n+1}{H}\left(1-\frac{\mathcal{Z}}{H}\right)^n \\ &= 2A\,\tau_b^n\,\left(1-\frac{\mathcal{Z}}{H}\right)^n.\end{aligned} \tag{S16}$$

The first-order Taylor series approximation of the velocity is then

$$\begin{aligned}v_{\mathcal{X}}(\mathcal{Z}) &= v(0) + \left.\frac{\mathrm{d}v_{\mathcal{X}}}{\mathrm{d}\mathcal{Z}}\right|_{\mathcal{Z}=0}\mathcal{Z} + \mathcal{O}(\mathcal{Z}^2) \\ &= 2A\,\tau_b^n\,\mathcal{Z} + \mathcal{O}(\mathcal{Z}^2),\end{aligned} \tag{S17}$$

where $\mathcal{O}(\mathcal{Z}^2)$ is the error term. In the 'xyz' coordinates, the vertical component of the bed–parallel velocity at the top of the void is now

$$\begin{aligned}v_z(h) &= \sin(\alpha)\,v(\mathcal{Z}=h) \\ &= 2A\,(\rho_i\,g)^n\,\sin^{n+1}(\alpha)\,H^n\,h.\end{aligned} \tag{S18}$$

FITTING OF NUMERICAL MODEL RESULTS

Fitting the analytical void-height approximation Eqn. (14) to the numerical model result is done in a few steps. Best-fit values of the coefficients and exponents were found using the `optimize.curve_fit` function, a non-linear least squares method that fits a function to data, from the python library SciPy (https://scipy.org/). To estimate a single set of constants for each of the four heat transport modes, the constants are determined in the order of c, b and a, from Eqn. (14). The exponent c is computed as the weighted mean of the values from each bed slope, c_α, with the number of steady state samples for each bed slope, N_α, as the weight:

$$c = \frac{\sum_\alpha c_\alpha\,N_\alpha}{\sum_\alpha N_\alpha}. \tag{S19}$$

Next, the best fit to the approximation is found again, but with the newly-determined exponent c given, and b is computed as the weighted mean, similarly to c. Finally, the value of a is determined by finding the best fit to the approximation, i.e. Eqn. (14), with the now determined exponents b and c given.

To complete the linear and physical forms of the approximation, coefficients $a_{\mathrm{L/P1}}$ and $a_{\mathrm{L/P2}}$ are then evaluated from the constant a, found in the previous step. The coefficients were determined for the best-fit

values of b and c, determined in the previous step, as well as their theoretical values. The result is four variations of the initial approximation, Eqn. (14): linear function of the sine of the bed slope for a and weighted means for b and c; linear function of the sine of the bed slope for a and theoretical values for b and c; theoretically derived slope-dependence for a and weighted means for b and c; and theoretically derived slope-dependence for a and theoretical values for b and c.

QUALITY OF VOID-HEIGHT APPROXIMATION

The relative error is generally higher for smaller voids (e.g., column 2 in Fig. S10b), as is to be expected due to how the relative error is computed. For approximations that used the best-fit values of b and c, relative error increases with bed slope, especially for smaller void heights (compare rows in Fig. S10a and S10c). However, the approximations that use the theoretical values of b and c have a more uniform, albeit elevated, error over the range of bed slopes and void heights examined (Fig. S10b and S10d). The maximum relative error for each heat transport mode is always lower using the theoretical values of b and c than using the best-fit values, but the average error is generally higher. For the approximations with fitted values of b and c, the mean and median relative error increase with bed slope for all heat transport modes except for M3, where it first dips before increasing (S1). The median relative error is less than the mean for nearly all simulation ensembles where heat-transport mode and bed slope are varied (S1). The median likely gives a better assessment of the quality of the approximations as it is not affected by the outliers generally associated with smaller void heights.

INFLUENCE OF PARAMETER CHANGES ON VOID HEIGHT

To investigate the relative importance of changes in glacier thickness and heat flux, we differentiate the established void-height approximation Eqn. (14) with respect to glacier thickness:

$$\begin{aligned} \frac{\partial}{\partial H}\frac{h}{H} &= a\,b\,H^{b-1}\,\dot{Q}^{c} \\ &= a\,H^{b}\,\dot{Q}^{c}\left(b\,H^{-1}\right) \\ &= \frac{h}{H}\left(b\,H^{-1}\right) \\ \partial\left(\frac{h}{H}\right)\Big/\frac{h}{H} &= b\frac{\partial H}{H}, \end{aligned} \tag{S20}$$

and with respect to heat flux:

$$\begin{aligned} \frac{\partial}{\partial \dot{Q}} \frac{h}{H} &= a\, c\, H^b\, \dot{Q}^{c-1} \\ &= a\, H^b\, \dot{Q}^c \left(c\, \dot{Q}^{-1} \right) \\ &= \frac{h}{H} \left(c\, \dot{Q}^{-1} \right) \\ \partial \left(\frac{h}{H} \right) \Big/ \frac{h}{H} &= c \frac{\partial \dot{Q}}{\dot{Q}}. \end{aligned} \tag{S21}$$

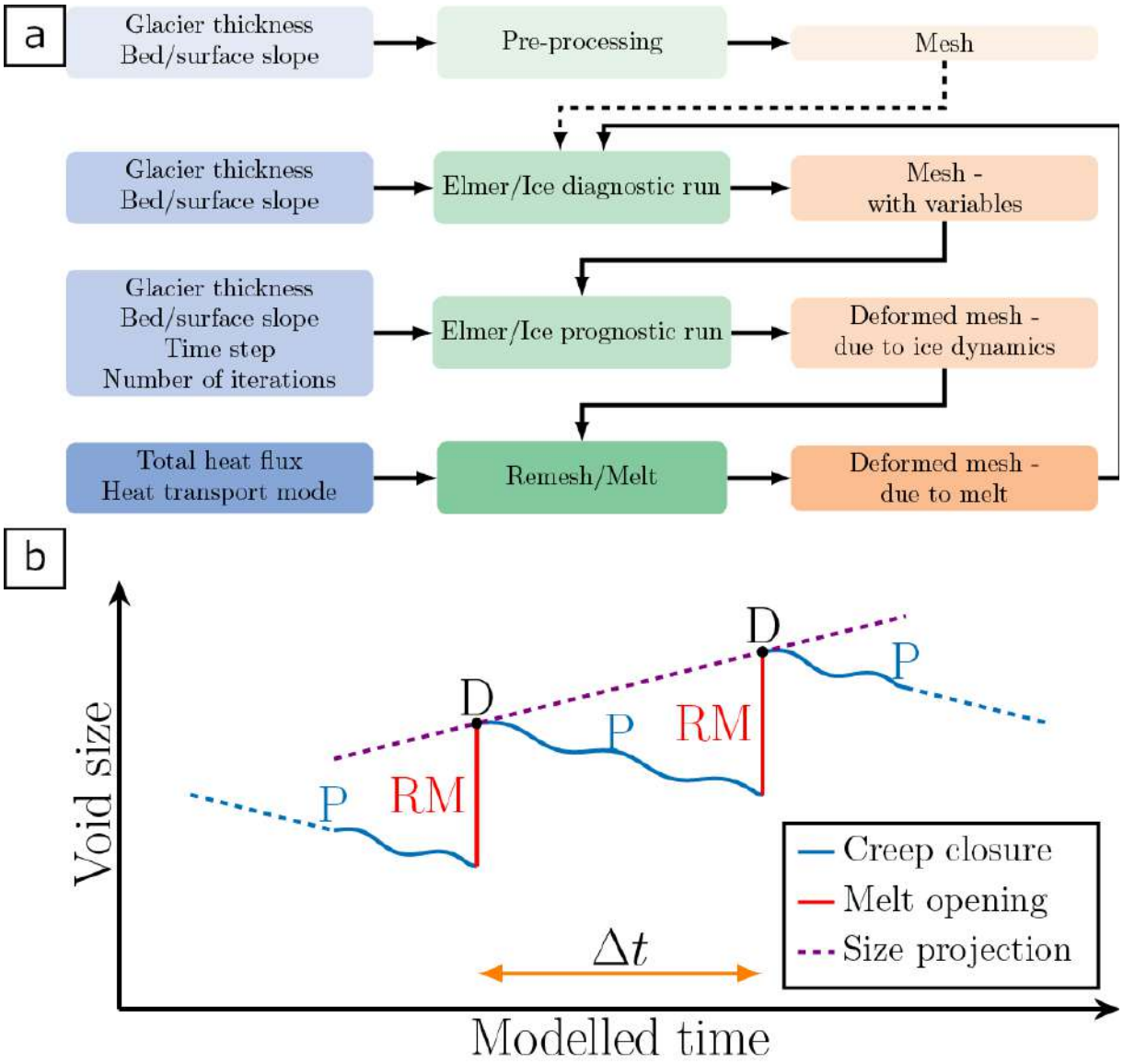

Fig. S3. (**a**) The model workflow, with each step in green boxes, inputs in blue boxes and outputs, which then feed into the next step, in orange boxes. Top line: preprocessing step initialises mesh and results files. The model domain is constructed as a rectangular slab of uniform ice thickness H and bed slope α. An initial void, shaped as a spherical cap, is prescribed in order for the model to be able to melt the overlying ice. Middle lines: Elmer/Ice (Gagliardini and others, 2013) used to model deformation of the domain due to ice dynamics, according to the full-Stokes solution of the ice-flow equation. Bottom line: python module where the geothermally induced melt is applied, using the four heat transport modes, and the domain is remeshed. (**b**) A schematic showing model progress, with model components D: Elmer/Ice diagnostic run; P: Elmer/Ice prognostic run; and RM: remesh/melt step. Creep closure is only considered during the prognostic step, while the melt is applied instantaneously thereafter. Each prognostic step runs for a total time of Δt, which is the sum of four smaller time steps the prognostic model iterates over.

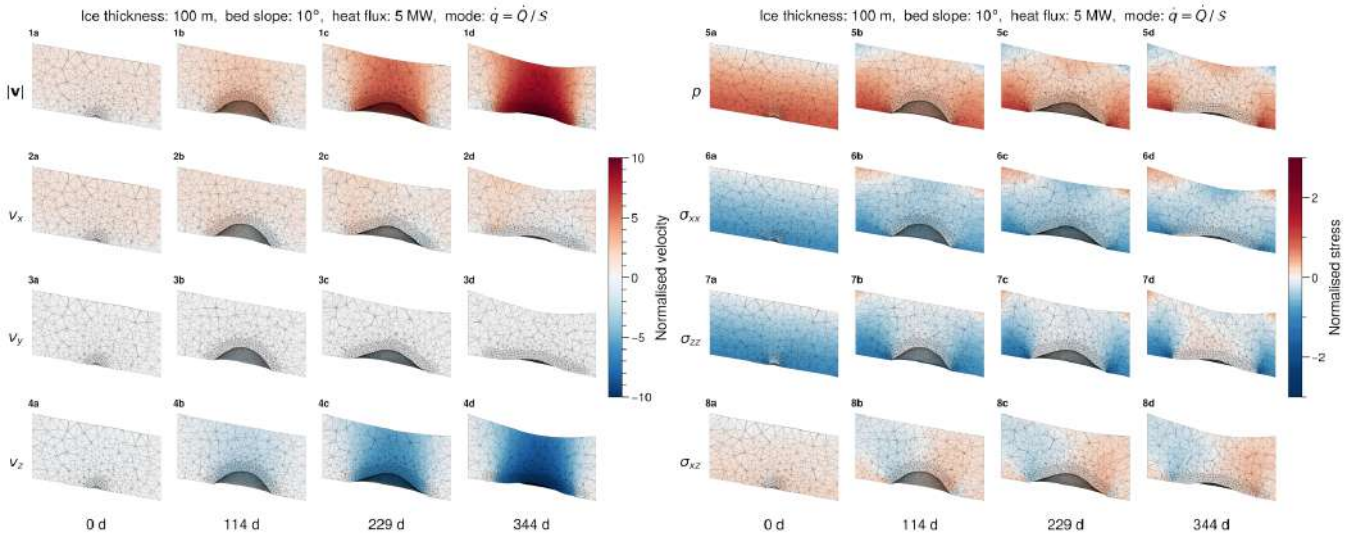

Fig. S4. Example of the evolution of the model domain for ice thickness $H = 100\,\mathrm{m}$, bed slope $\alpha = 10°$, heat flux $\dot{Q} = 5.0\,\mathrm{MW}$ and heat transport mode M1. The figures on the left show velocity magnitude, $|\mathbf{v}|$, and x, y and z components. The velocities are normalised to the maximum velocity given by the shallow ice approximation Eqn. (10), $v_{\mathrm{SIA}} = v_{\mathcal{X}}(\mathcal{Z} = H)$. The figures on the right show the pressure and the xx, zz and xz component of the stress, i.e. σ_{xx}, σ_{zz} and σ_{xz}. The stresses are normalised to the maximum ice overburden pressure p_{i}. Note that the figures are only meant to show equally spaced snapshots through the entire timeseries, but not the evolution towards a steady state.

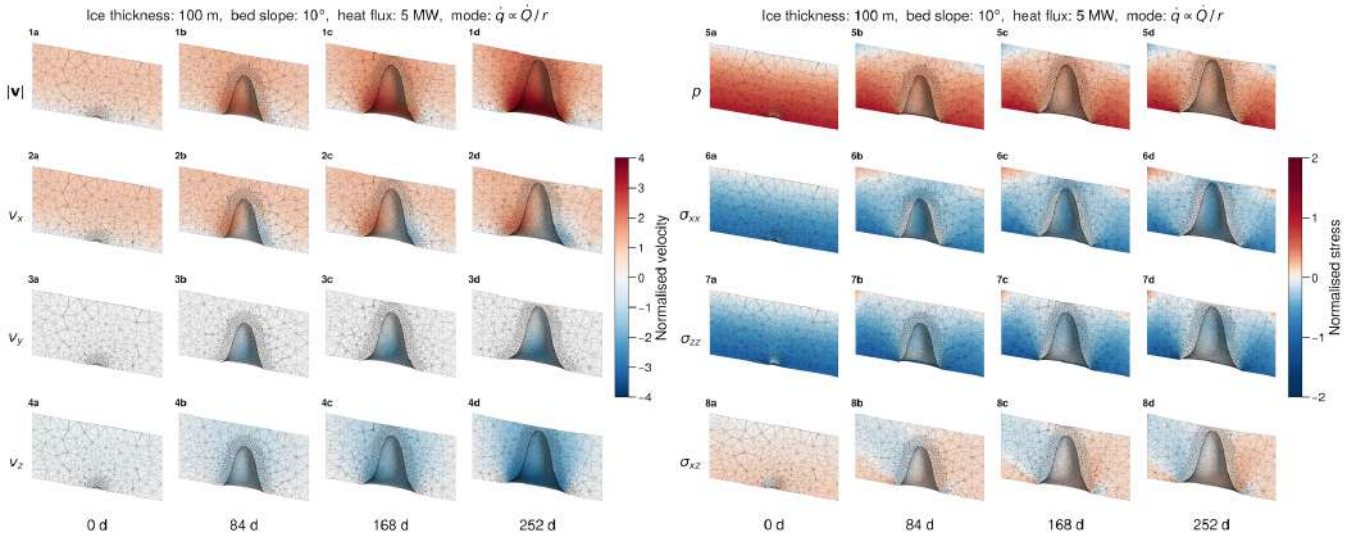

Fig. S5. Example of the evolution of the model domain for ice thickness $H = 100\,\mathrm{m}$, bed slope $\alpha = 10°$, heat flux $\dot{Q} = 5.0\,\mathrm{MW}$ and heat transport mode M2. The figures on the left show velocity magnitude, $|\mathbf{v}|$, and x, y and z components. The velocities are normalised to the maximum velocity given by the shallow ice approximation Eqn. (10), $v_{\mathrm{SIA}} = v_{\mathcal{X}}(\mathcal{Z} = H)$. The figures on the right show the pressure and the xx, zz and xz component of the stress, i.e. σ_{xx}, σ_{zz} and σ_{xz}. The stresses are normalised to the maximum ice overburden pressure p_{i}. Note that the figures are only meant to show equally spaced snapshots through the entire timeseries, but not the evolution towards a steady state.

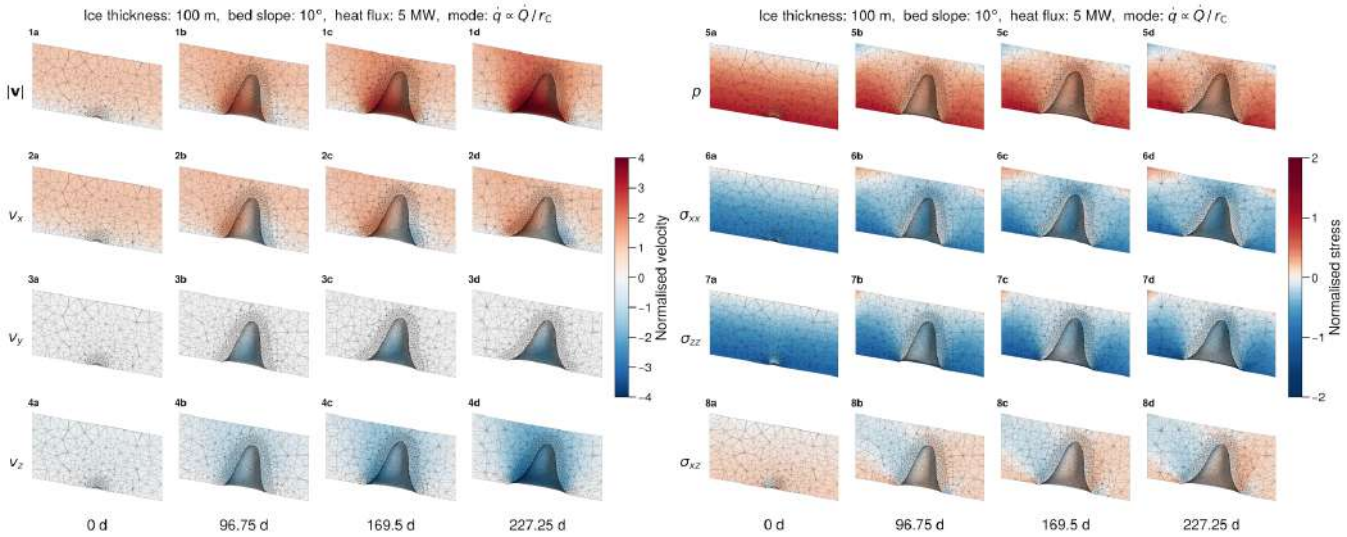

Fig. S6. Example of the evolution of the model domain for ice thickness $H = 100\,\mathrm{m}$, bed slope $\alpha = 10°$, heat flux $\dot{Q} = 5.0\,\mathrm{MW}$ and heat transport mode M3. The figures on the left show velocity magnitude, $|\mathbf{v}|$, and x, y and z components. The velocities are normalised to the maximum velocity given by the shallow ice approximation Eqn. (10), $v_{\mathrm{SIA}} = v_{\mathcal{X}}(\mathcal{Z} = H)$. The figures on the right show the pressure and the xx, zz and xz component of the stress, i.e. σ_{xx}, σ_{zz} and σ_{xz}. The stresses are normalised to the maximum ice overburden pressure pi. Note that the figures are only meant to show equally spaced snapshots through the entire timeseries, but not the evolution towards a steady state.

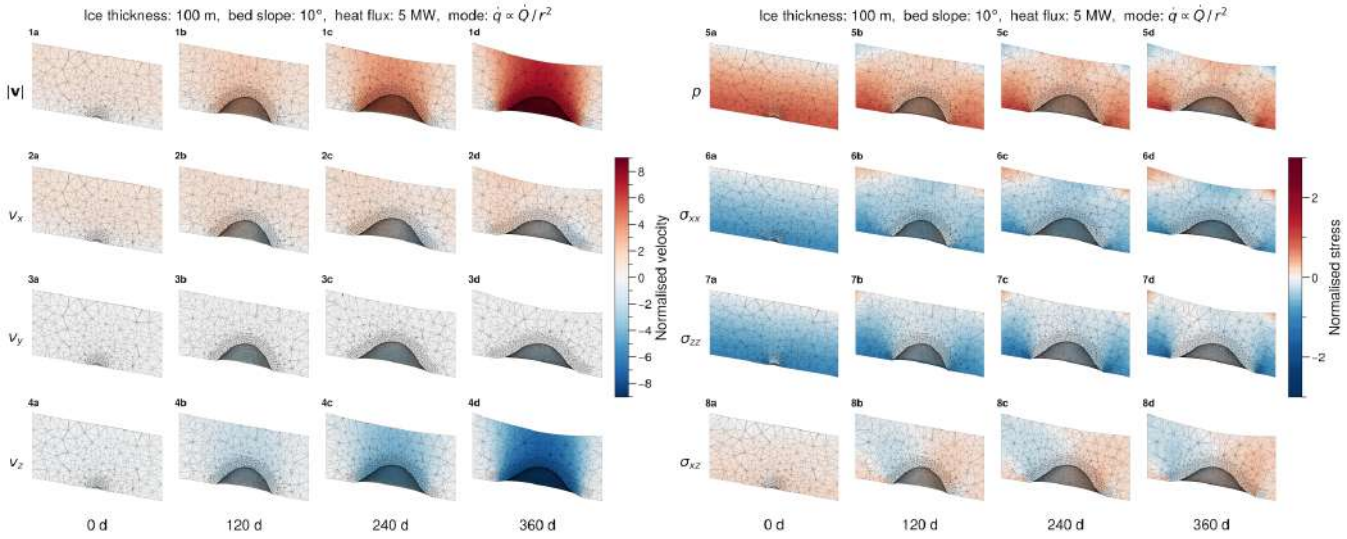

Fig. S7. Example of the evolution of the model domain for ice thickness $H = 100\,\mathrm{m}$, bed slope $\alpha = 10°$, heat flux $\dot{Q} = 5.0\,\mathrm{MW}$ and heat transport mode M4. The figures on the left show velocity magnitude, $|\mathbf{v}|$, and x, y and z components. The velocities are normalised to the maximum velocity given by the shallow ice approximation Eqn. (10), $v_{\mathrm{SIA}} = v_{\mathcal{X}}(\mathcal{Z} = H)$. The figures on the right show the pressure and the xx, zz and xz component of the stress, i.e. σ_{xx}, σ_{zz} and σ_{xz}. The stresses are normalised to the maximum ice overburden pressure pi. Note that the figures are only meant to show equally spaced snapshots through the entire timeseries, but not the evolution towards a steady state.

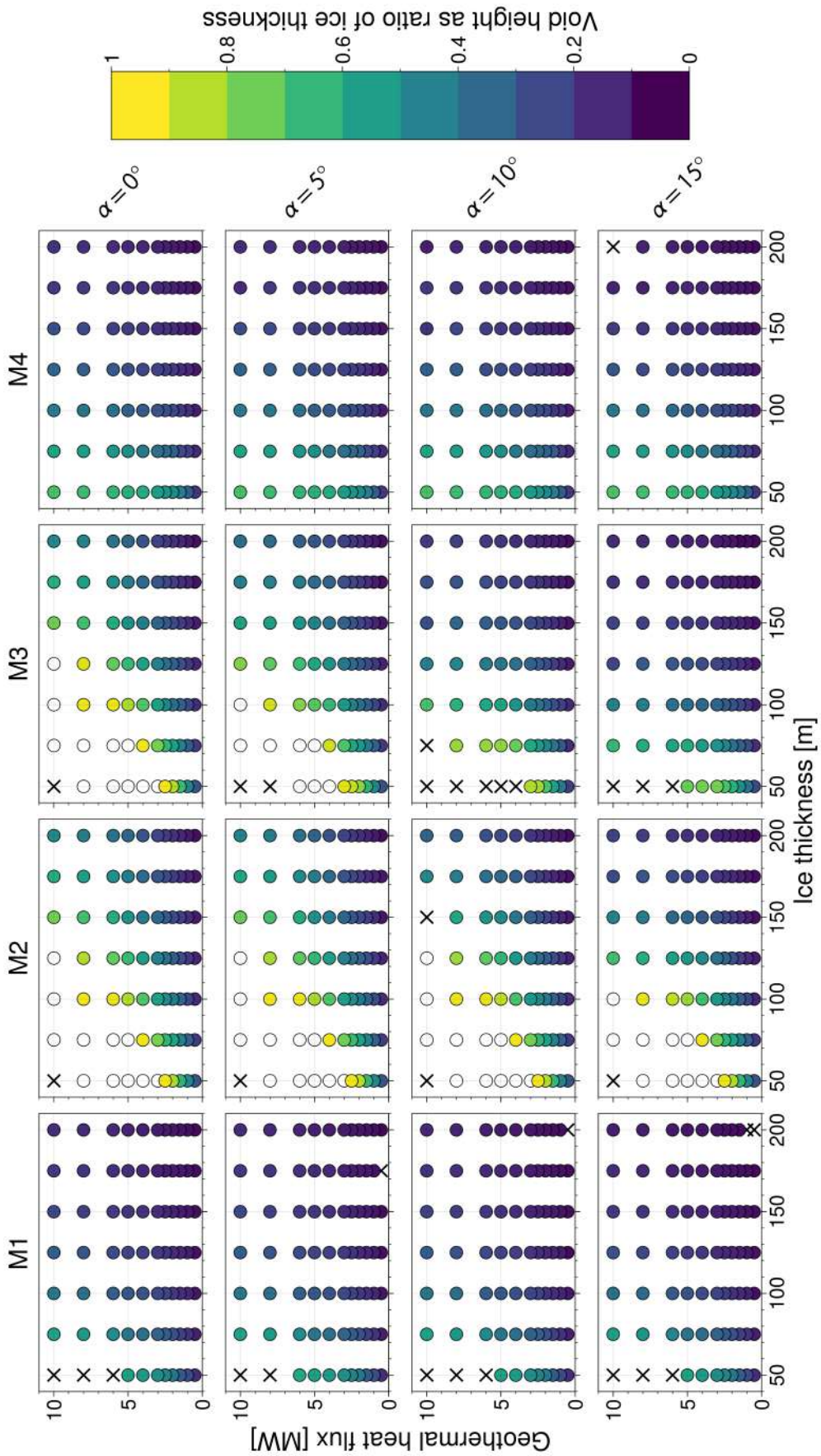

Fig. S8. Steady-state heights of the simulated glaciovolcanic voids. Model simulation results are shown as filled circles, **x**'s indicate simulations that did not reach steady state, or failed otherwise, and the white circles are the non-steady-state simulation results where void height exceeded 90 % of ice thickness.

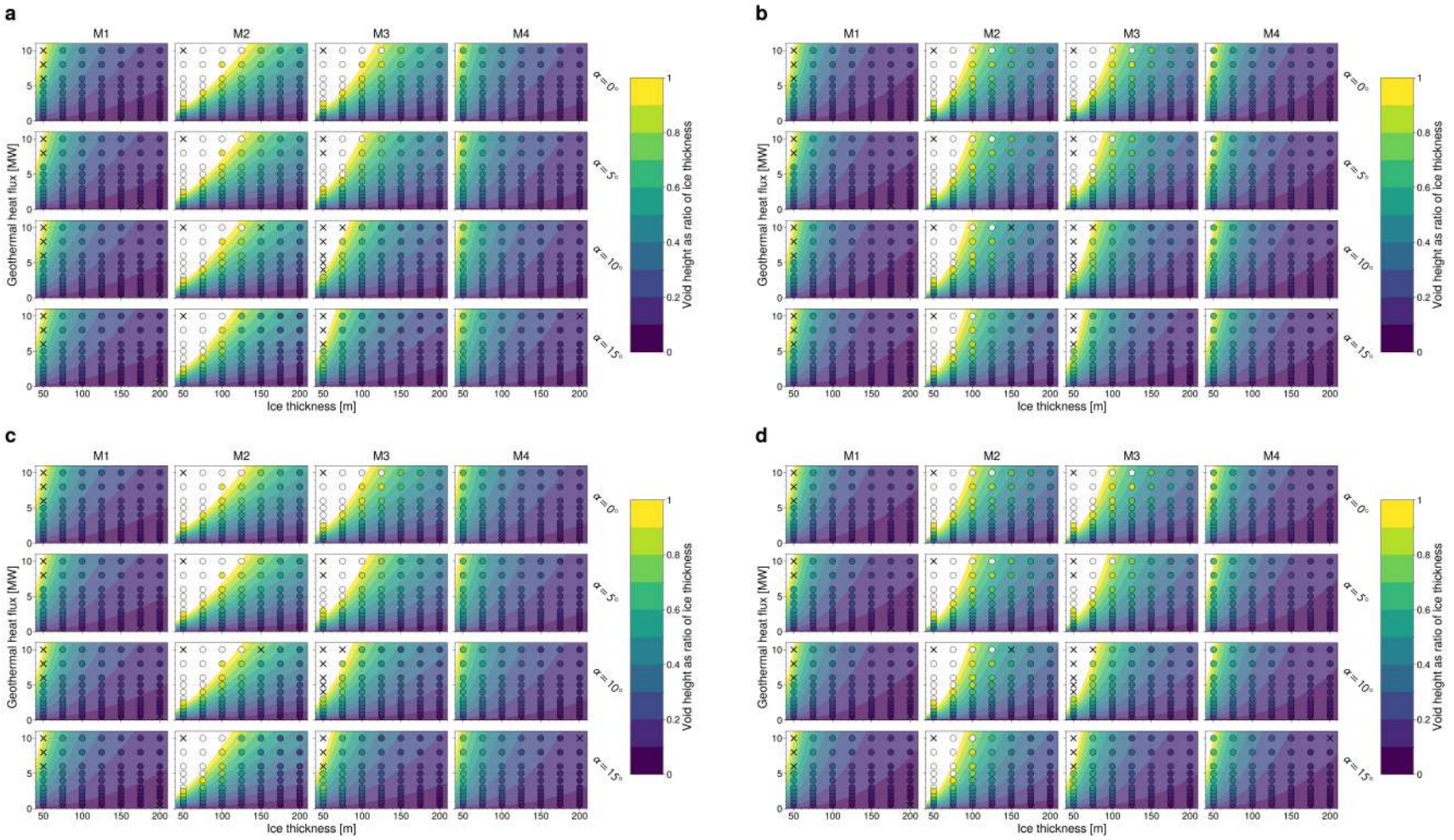

Fig. S9. Analytical approximations of the modelled steady-state void heights. Model simulation results are shown as filled circles overlying contours of the analytical approximations. **X**'s indicate simulations that did not reach steady state, or failed otherwise, and the white cicles are the non-steady-state simulation results where void height exceeded 90 % of ice thickness. All approximations are of the form: $h/H = a\,H^b\,\dot{Q}^c$, with constant a taking the form $a = a_1(1 + a_2\,\sin(\alpha))$ in panels (**a**) and (**b**), and $a = a_1\left(1 + a_2\,\sin^{n+1}(\alpha)\right)^{-\frac{1}{2}}$ in panels (**c**) and (**d**). Approximations in (**a**) and (**c**) use best-fit values of b and c, while those in (**b**) and (**d**) use theoretical values (see Table S1).

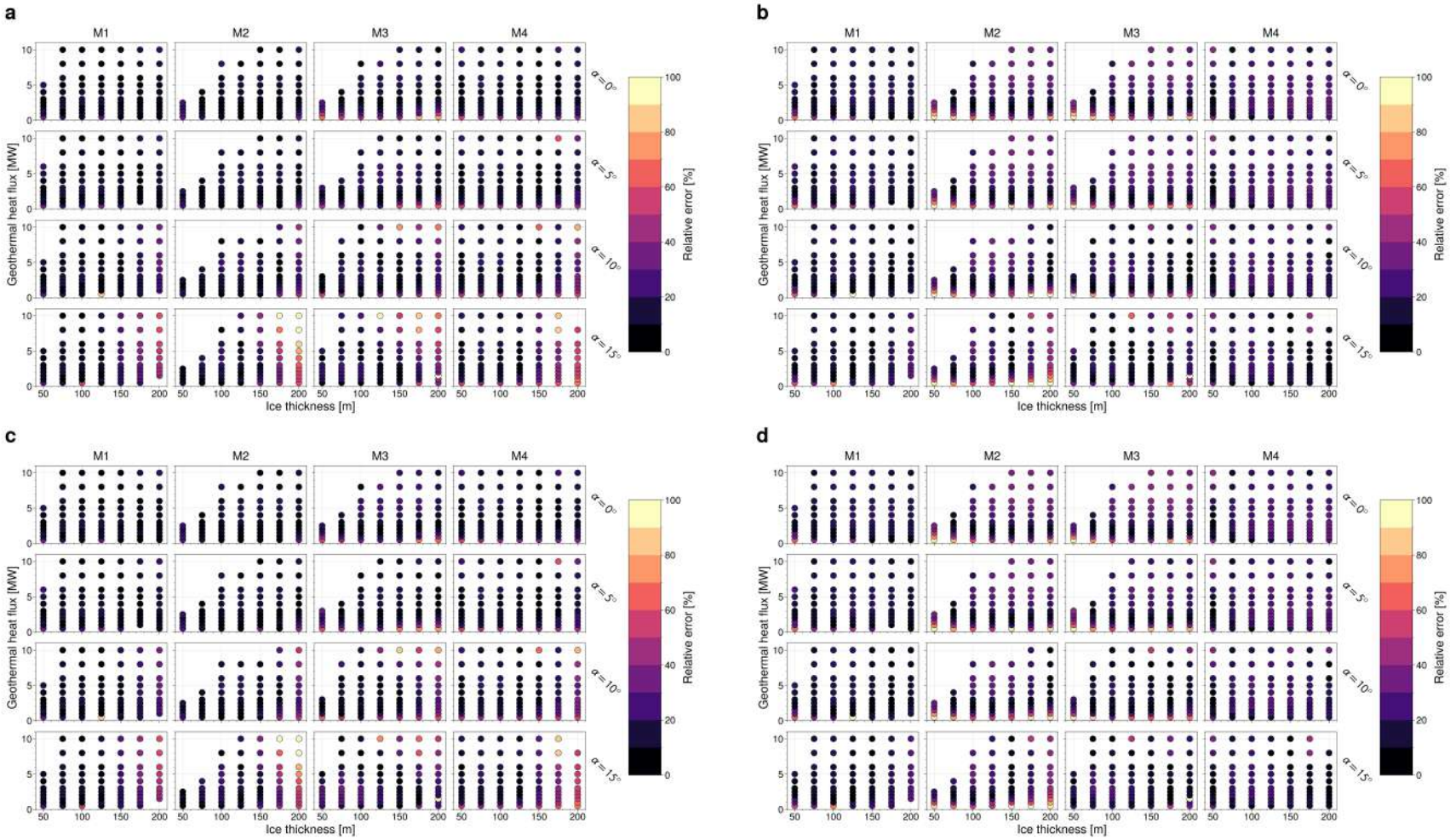

Fig. S10. Relative error of the approximated steady state void heights compared to the simulated steady states (coloured circles). Blank spaces indicate non-steady state simulations that either melted above 90 % of the ice thickness or were not completed. All approximations are of the form: $h/H = a\,H^b\,\dot{Q}^c$, with constant a taking the form $a = a_1(1 + a_2\,\sin(\alpha))$ in panels (**a**) and (**b**), and $a = a_1\left(1 + a_2\,\sin^{n+1}(\alpha)\right)^{-\frac{1}{2}}$ in panels (**c**) and (**d**). Approximations in (**a**) and (**c**) use best-fit values of b and c, while those in (**b**) and (**d**) use theoretical values (see Table S1).

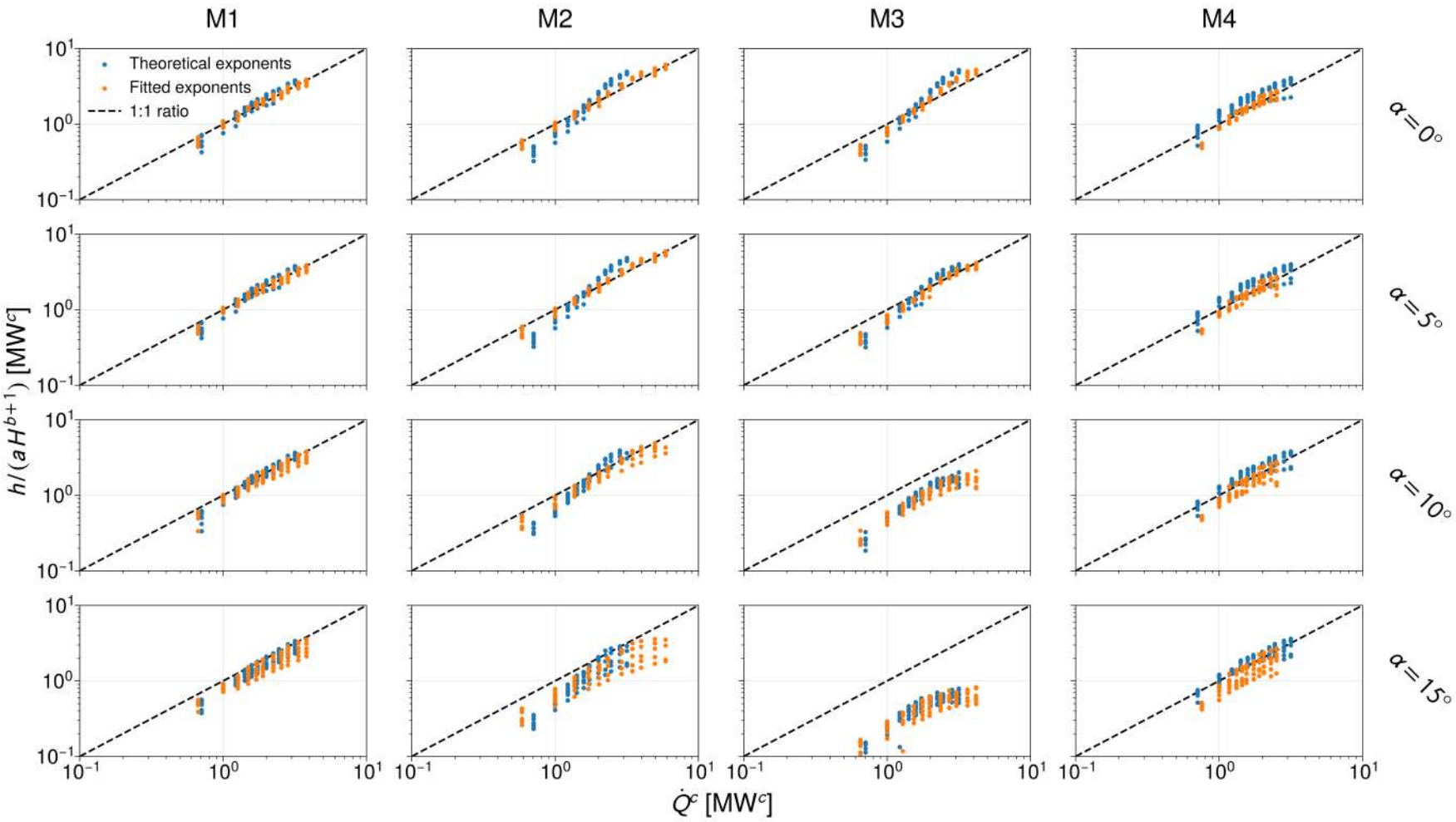

Fig. S11. The scaling collapse of the numerical model results to the general void-height approximation Eqn. (14): $h/H = a\,H^b\,\dot{Q}^c$. The theoretical values of the exponents, $b = -n/2$ and $c = 1/2$ are shown in blue, and the respective best fitted values (Table S1) are shown in orange. The value of a is taken for the physical approximations Eqn. (S14).

Table S1. Values of constants a_1, a_2, b, c for the linear and physical approximations, that link glaciovolcanic void height, h, to glacier thickness, H, and the total heat flux, $\dot{Q}$. For each approximation and each heat transport mode, constants a_1 and a_2 are determined for both the best-fitted and theoretical values of b and c. The mean and median relative errors of the approximations compared to the simulation results, for each given combination of constants a_1, a_2, b and c, are given as a function of bed slope. (0°–15°).

Approximation	Mode	Constants				Mean error [%]				Median error [%]			
		$a_{\mathrm{L/P1}}$ [$\mathrm{m}^{-b}\mathrm{MW}^{-c}$]	$a_{\mathrm{L/P2}}$	b	c	0°	5°	10°	15°	0°	5°	10°	15°
Equation A28:	M1	46.08	-0.20	-1.32	0.58	6.6	8.0	11.9	18.9	5.4	6.4	9.0	12.1
	M2	109.90	-0.65	-1.34	0.77	7.4	8.7	13.3	29.8	4.8	7.1	10.6	16.6
	M3	115.71	-2.02	-1.31	0.62	19.1	14.7	16.9	25.2	13.7	12.0	12.2	17.5
$a_{\mathrm{L1}}\,(1 + a_{\mathrm{L2}}\,\sin(\alpha))\;H^b\,\dot{Q}^c$	M4	30.69	-0.12	-1.15	0.40	11.8	13.6	19.0	26.6	8.4	9.5	13.4	17.8
	M1	109.88	-0.18	-1.50	0.50	13.6	13.9	11.6	14.4	12.8	11.8	8.7	11.2
	M2	301.26	-0.51	-1.50	0.50	27.5	27.7	26.4	33.4	24.0	25.7	21.0	24.0
	M3	302.25	-1.90	-1.50	0.50	28.5	25.6	16.8	17.5	23.6	24.6	11.7	10.8
	M4	112.10	-0.09	-1.50	0.50	22.5	22.0	18.9	13.5	24.2	23.7	19.8	11.7
Equation A33:	M1	45.54	23.21	-1.32	0.58	7.0	8.9	12.2	18.5	5.9	6.1	8.7	12.5
	M2	106.55	104.96	-1.34	0.77	7.7	8.3	14.3	27.8	6.1	6.4	9.6	18.4
	M3	106.78	850.72	-1.31	0.62	16.9	16.6	20.1	21.3	15.1	10.2	12.9	18.6
$a_{\mathrm{P1}}\left(1 + a_{\mathrm{P2}}\,\sin^{n+1}(\alpha)\right)^{-\frac{1}{2}}\;H^b\,\dot{Q}^c$	M4	30.48	13.86	-1.15	0.40	11.7	13.6	19.4	26.3	8.5	9.3	14.3	17.2
	M1	108.72	19.73	-1.50	0.50	14.2	13.7	11.7	14.1	13.5	11.0	8.8	11.4
	M2	293.47	73.41	-1.50	0.50	27.0	27.0	27.9	31.7	24.9	24.5	20.6	23.6
	M3	278.79	700.29	-1.50	0.50	27.4	26.1	18.5	15.2	26.0	21.9	10.9	11.8
	M4	111.55	9.98	-1.50	0.50	22.8	21.8	18.6	13.7	24.6	23.5	19.3	12.0

REFERENCES

Cuffey KM and Paterson WSB (2010) *The Physics of Glaciers*. Butterworth-Heinemann – Elsevier, Oxford, fourth edition, ISBN 978-0-12-369461-4

Farinotti D, Huss M, Fürst JJ, Landmann J, Machguth H, Maussion F and Pandit A (2019) A consensus estimate for the ice thickness distribution of all glaciers on Earth. *Nature Geoscience*, **12**(3), 168–173 doi: 10.1038/s41561-019-0300-3

Gagliardini O, Zwinger T, Gillet-Chaulet F, Durand G, Favier L, de Fleurian B, Greve R, Malinen M, Martín C, Råback P, Ruokolainen J, Sacchettini M, Schäfer M, Seddik H and Thies J (2013) Capabilities and performance of Elmer/Ice, a new-generation ice sheet model. *Geoscientific Model Development*, **6**(4), 1299–1318 doi: 10.5194/gmd-6-1299-2013

Millan R, Mouginot J, Rabatel A and Morlighem M (2022) Ice velocity and glacier thickness of the world's glaciers. *Nature Geoscience*, **15**(2), 124–129 doi: 10.1038/s41561-021-00885-z

Nye JF (1953) The flow law of ice from measurements in glacier tunnels, laboratory experiments and the Jungfraufirn borehole experiment. *Proceedings of the Royal Society of London. Series A. Mathematical and Physical Sciences*, **219**(1139), 477–489 doi: 10.1098/rspa.1953.0161

Planet Team (2015) Planet Application Program Interface: In Space for Life on Earth Available at https://api.planet.com

Warwick R (2020) *A comprehensive volcanic hazard assessment for Mount Meager Volcanic Complex, B.C.* Master's thesis, Simon Fraser University Available at https://summit.sfu.ca/item/34375

White RH, Anderson S, Booth JF, Braich G, Draeger C, Fei C, Harley CDG, Henderson SB, Jakob M, Lau CA, Admasu LM, Narinesingh V, Rodell C, Roocroft E, Weinberger KR and West G (2023) The unprecedented Pacific Northwest heatwave of June 2021. *Nature Communications*, **14**(1), 727, ISSN 2041-1723 doi: 10.1038/s41467-023-36289-3

Williams-Jones G (2016) Status of the Mount Meager Volcanic Complex, BC, Canada. Technical report, VolCan Geoconsulting

Williams-Jones G and Rymer H (2015) Hazards of volcanic gases. In H Sigurdsson (ed.), *Encyclopedia of volcanoes*, chapter 57, 985–992, Academic Press, second edition doi: 10.1016/B978-0-12-385938-9.00057-2